Recent progress in slope-assisted Brillouin optical correlation-domain reflectometry

Heeyoung Lee,[a] Kentaro Nakamura,[b] and Yosuke Mizuno[c*]

[a]*College of Engineering, Shibaura Institute of Technology, Tokyo 135-8548, Japan*

[b]*Institute of Innovative Research, Tokyo Institute of Technology, Yokohama 226-8503, Japan*

[c]*Faculty of Engineering, Yokohama National University, Yokohama 240-8501, Japan*

*Corresponding author.
E-mail addresses: hylee@shibaura-it.ac.jp (H. Lee), knakamur@sonic.pi.titech.ac.jp (K. Nakamura), mizuno-yosuke-rg@ynu.ac.jp (Y. Mizuno).

Abstract

Brillouin optical correlation-domain reflectometry (BOCDR) is one of the fiber-optic Brillouin-based distributed sensing techniques for strain and temperature with single-end accessibility. Since the first proposal of the basic concept in 2008, the performance of BOCDR has been drastically improved from a variety of aspects including high-speed operation. Here, we focus on one of the high-speed BOCDR configurations referred to as slope-assisted (SA-) BOCDR. In this configuration, instead of observing the whole Brillouin gain spectrum, only the spectral power at a certain frequency on the spectrum is detected, leading to frequency-sweep-free high-speed operation and some unique features. In this review paper, we describe the recent advances of SA-BOCDR technology from its principle to characterization and applications. We also discuss the current issues of SA-BOCDR and present a concluding remark.

Keywords: Optical fiber sensors; Distributed sensing; Brillouin scattering; Optical reflectometry; Correlation-domain technique; Structural health monitoring

1. Introduction

Distributed strain and temperature sensing based on Brillouin scattering in optical fibers has been gathering a lot of attention for several decades as a promising technique for structural health monitoring of civil infrastructures, such as buildings, bridges, tunnels, dams, pipelines, railways, and many others. To date, a variety of methods have been implemented to acquire the information on Brillouin gain spectrum (BGS) distributions, from which the magnitude and position of strain or temperature change can be derived [1]. One of the most widely used techniques is a time-domain technique, which includes Brillouin optical time-domain analysis (BOTDA) [2–17] and Brillouin optical time-domain reflectometry (BOTDR) [18–25]. Their performance has been dramatically enhanced, and even sub-centimeter spatial resolution and real-time operation have been achieved. Another Brillouin-based distributed sensing technique is a correlation-domain technique, which include Brillouin optical correlation-domain analysis (BOCDA) [26–40] and Brillouin optical correlation-domain reflectometry (BOCDR) [41–65]. These techniques have not only sub-centimeter spatial resolution but also a unique advantage of random accessibility to measuring points. With this feature, strain or temperature sensing at specific points along a fiber under test (FUT) can be measured with an extremely high sampling rate. BOCDA is based on stimulated Brillouin scattering (SBS) and higher-power Brillouin signal can be used in the system, light needs to be injected into both ends of the FUT. In contrast, BOCDR utilizes spontaneous Brillouin signal with lower signal power, it operates by light injection into only one end of the FUT. Then, even when the FUT is broken during operation, distributed measurement can be continued in the range from the

proximal end of the FUT to the breakage point. Hereafter, we focus on BOCDR technique.

BOCDR operates on the basis of a synthesized optical coherence function (SOCF) [66]. In a standard configuration, the optical frequency of a laser output is modulated sinusoidally to generate a so-called correlation peak (corresponding to a sensing position) in the FUT. By scanning the correlation peak along the FUT and observing the BGS at every point, distributed measurement of Brillouin frequency shift (BFS), which gives the information of strain and temperature, can be performed. To date, we have drastically improved the performance of BOCDR, including enhancement of spatial resolution [44–46], extension of measurement range [47–49], improvement of measurement stability [50–53], widening of the strain dynamic range [54], simplification of the system setup [55–57], reduction of implementation cost [58,59], and use of polymer optical fibers (POFs) [52,53,57,60]. The operation speed is also the target of performance improvement. A conventional BOCDR configuration required a longer measurement time because frequency-sweeping-based BGS observation was needed at every sensing point along the FUT, which made it difficult to perform real-time distributed measurement. To overcome this drawback, we have recently developed two frequency-sweeping-free configurations of BOCDR, called phase-detected (PD-) BOCDR [61,62] and slope-assisted (SA-) BOCDR [67]. Note that PD-BOCDR has been well reviewed in our recent paper [62].

In this paper, we review SA-BOCDR from its fundamental operating principle to its unique features and application examples. We also discuss the technical issues to be resolved in future.

2. Principle of SA-BOCDR

First of all, we describe the basic principle of standard BOCDR. In BOCDR, the pump light and the reference light are sinusoidally modulated, and correlation peaks are generated in the FUT. In a standard configuration, we adjust the modulation parameters so that only one correlation peak is located in the FUT. By sweeping the correlation peak along the FUT, distributed BFS measurement is feasible. The measurement range d_m is determined by the interval of the neighboring correlation peaks as [41,43]

$$d_m = \frac{v_g}{2 f_m}, \tag{1}$$

where v_g is the group velocity of light and f_m is the modulation frequency. The spatial resolution Δz is given by [41,43]

$$\Delta z = \frac{v_g \Delta \nu_B}{2\pi f_m \Delta f}, \tag{2}$$

where $\Delta \nu_B$ is the Brillouin gain bandwidth (~ 30 MHz in silica fibers) and Δf is the modulation amplitude of the light source. It is clear from Eqs. (1) and (2) that the measurement range and the spatial resolution are in a trade-off relation in terms of the modulation frequency f_m.

In standard BOCDR, the BFS at a single sensing point is derived after acquiring the whole BGS. In contrast, SA-BOCDR detects the BFS information using the BGS slope [67]. Note that this idea itself was not new; some examples of SA-BOTDA are found [11–15]. As depicted in Fig. 1(a), the BFS is in one-to-one correspondence with the spectral power P_{B0} at a certain frequency ν_{B0}, which is set at the high-frequency point in the linear region (lower-frequency side) of the BGS slope. Then, when the BFS slightly shifts to higher frequency by strain and temperature, P_{B0} decreases linearly; when the slight loss occurs in the FUT, the spectral power of the BGS entirely decreases, also leading to the reduction of P_{B0}. This sensitivity to optical loss is sometimes an advantage but sometimes a disadvantage (the countermeasure in the latter case will be described in Section 5). Figures 1(b) and 1(c) show the changes in the P_{B0} distributions when strain (or heat) and loss are locally applied, respectively. The strain and heat effects cannot be separated in this method, but the loss effect can be discriminated from the locally applied strain (or heat) in some cases, because the decreased P_{B0} value does not return to the initial value. The P_{B0} change distributions, which are calculated by substituting the resultant P_{B0} distributions (solid curves) from their initial distributions (dotted lines), are often used as final measurement results. The optimal ν_{B0} value can be calculated by differentiating the measured BGS. In a standard silica single-mode fiber (SMF) with a BFS of 10.89 GHz, the optimal ν_{B0} value was 10.85 GHz.

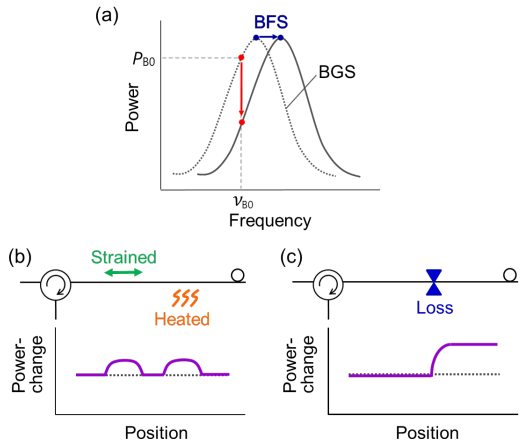

Fig. 1. Operating principle of SA-BOCDR. (a) One-to-one correspondence between the BFS and the spectral power P_{B0} at frequency ν_{B0}. (b) P_{B0} distributions along the FUT with (solid curve) and without (dotted line) strain and heat. (c) P_{B0} distributions along the FUT with (solid curve) and without (dotted line) local loss.

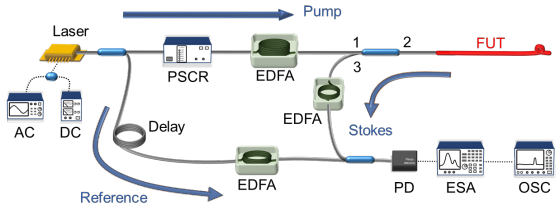

Fig. 2. Experimental setup of SA-BOCDR. AC, alternating current; DC, direct current; EDFA, erbium-doped fiber amplifier; ESA, electrical spectrum analyzer; FUT, fiber under test; OSC, oscilloscope; PD, photodiode; PSCR, polarization scrambler.

For more calculation details, refer to [67].

Figure 2 depicts the basic setup of SA-BOCDR, which is identical to that of standard BOCDR except for the final signal processing. The output light from a laser is divided into two: pump and reference. The pump light is amplified using an erbium-doped fiber amplifier (EDFA) and injected into the FUT. After propagating through a delay fiber (to control the order of the correlation peak) and another EDFA, the reference light is used for heterodyne detection with the Stokes light, which is also amplified using still another EDFA. The polarization-dependent fluctuations are suppressed using a polarization scrambler (PSCR). The heterodyned optical signal is converted into an electrical signal using a photodiode (PD) and guided to an electrical spectrum analyzer (ESA). Using a narrowband-pass filtering function of the ESA, the P_{B0} change at a fixed frequency ν_{B0} is sequentially output to an oscilloscope (OSC).

3. Characterization

In this Section, we describe some features unique to SA-BOCDR. A beyond-nominal-resolution effect [68,69], which is the ability to detect hotspots shorter than nominal spatial resolution, is one of the most interesting features, but we have already reviewed this effect in [42]. In this paper, we focus attention on other unique features, such as the measurement sensitivity dependencies on experimental conditions [70] and the trade-off relationship between strain dynamic range and spatial resolution [71].

3.1. Sensitivity dependencies on incident power and spatial resolution

As explained in Section 2, the measurement sensitivity of SA-BOCDR is determined by the slope of the BGS, which depends on the change in incident light power and spatial resolution. It is thus important to clarify the sensitivity dependencies on these experimental conditions. We analyzed the BGS shape and measured the sensitivity dependencies on the incident power and the spatial resolution [70].

Examples of the BGS measured at incident powers of 15 and 24 dBm at various spatial resolutions are shown in Figs. 3(a) and 3(b), respectively. The FUT was a 3.0-m-long silica SMF. At both powers, the BGS gradually grew weaker and broader as the spatial resolution became higher, leading to the reduced spectral slope. We then analyzed the spectral slopes of each BGS and measured the sensitivity dependence on spatial resolution. Figure 4 plots the measurement sensitivities as functions of spatial resolution at different incident powers. Irrespective of the incident power, the measurement sensitivity was

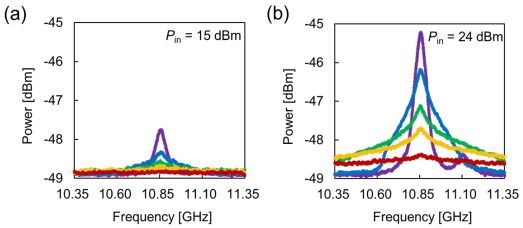

Fig. 3. BGS measured when the spatial resolution was 1.65 (purple), 0.43 (aqua), 0.18 (green), 0.09 (yellow), and 0.03 m (red). The incident powers were (a) 15 dBm and (b) 24 dBm.

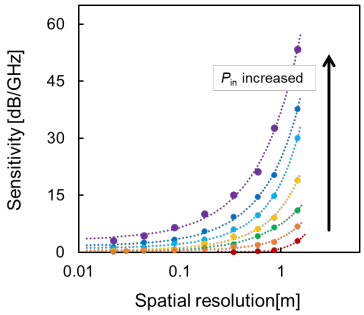

Fig. 4. Sensitivities plotted as functions of the spatial resolution at incident powers from 9 to 27 dBm with a step of 3 dB.

reduced and converged to 0 dB/GHz as the spatial resolution became higher.

This result was experimentally shown to be applicable by performing distributed temperature measurements, and higher-power light was confirmed to be preferable for enhanced measurement sensitivity as well as improved signal-to-noise ratio (SNR). However, excessive high-power light injection may cause what we call an optical fiber fuse effect [72,73]. Therefore, the optimal incident power will be ~25 dBm (for instance), depending on the actual conditions.

3.2. Trade-off relation between strain dynamic range and spatial resolution

One of the important issues unsolved yet is its strain (or temperature) dynamic range limited by the narrow linear range of the BGS slope. The linear

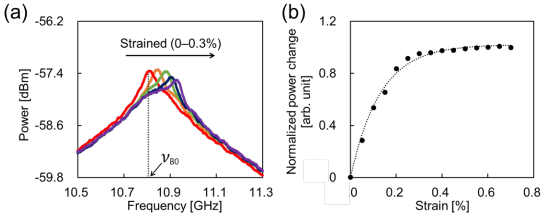

Fig. 5. (a) BGSs measured at strains of 0, 0.1, 0.2, 0.25, 0.3% when the strained length L_ε was the same as the nominal spatial resolution Δz (= ~0.37 m). (b) Normalized power change plotted as a function of applied strain. The dotted curve is an exponential fit.

range is generally reported to be several tens of megahertz, corresponding to a small strain of ~0.15% (or temperature change of ~64 K). We need to admit that this value is insufficient for many of practical applications.

The strain dynamic range of SA-BOCDR is generally determined by the linear range of the BGS slope. Then, it may be feasible to widen the dynamic range if the nonlinear range (foot of the BGS) is also used to measure strain at the cost of the reduced sensitivity. However, this method is not fully effective because of the bell-shaped background noise floor unique to the BGS in correlation-domain sensors [38]. This noise structure is caused by the Brillouin signals accumulated from non-correlated sections along the FUT. As most of the nonlinear range is composed of this noise, the strain dynamic range cannot be largely improved by this method.

We focused our attention on the fact that the noise structure mainly consists of the Brillouin signals from the non-sensing—but close to the sensing—sections. Therefore, by intentionally lowering the spatial resolution and including initially non-sensing sections into newly defined sensing sections, the noise floor will be drastically suppressed. Consequently, the strain dynamic range will be largely extended. In this meaning, SA-BOCDR possesses a trade-off relation between strain dynamic range and spatial resolution.

This scheme was experimentally demonstrated using a 7.5-m-long silica SMF. Refer to [71] for detailed conditions. When the strained length was identical to the spatial resolution, the strain dynamic

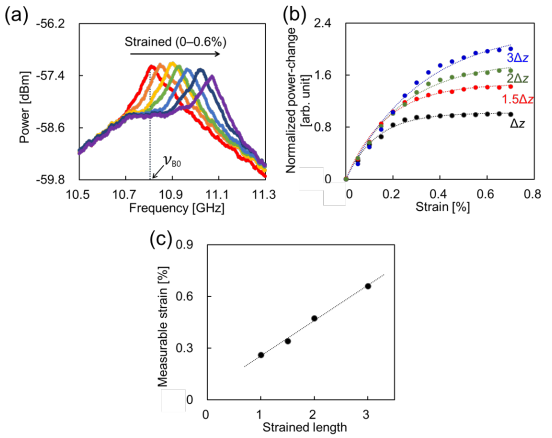

Fig. 6. (a) BGSs measured at strains of 0 to 0.6% (step: 0.1%) when the strained length was $3\Delta z$, where Δz is ~0.37 m. (b) Power changes plotted as functions of strain when the strained length was Δz, $1.5\Delta z$, $2\Delta z$, and $3\Delta z$. The dotted curves are exponential fits. (c) Maximal measurable strain plotted as a function of strained length. The dotted line is a linear fit.

range was 0.25% (with sensitivity lowered at 0.15–0.25%), as shown in Figs. 5(a) and 5(b). In contrast, when the strained length was longer than the nominal resolution, the strain dynamic range was much wider, as shown in Figs. 6(a) and 6(b). Figure 6(c) plots the measurable strain as a function of the strained length (divided by the resolution), which clearly indicates the trade-off relation between the strain dynamic range and the spatial resolution.

4. Demonstrations and Applications

Toward practical applications of SA-BOCDR, we conducted numerous demonstrations. First, we tested whether a POF can be employed as the FUT [74]. We then showed the usefulness of this system by a pseudo-field test [75]. We also demonstrated distributed temperature sensing with a long range of >10 km [76] along with bending-loss-independent operation [77] and stability/sensitivity-enhanced operation [78]. In addition, we used this system to measure the distribution of polarization beat length. In this Section, these topics are described.

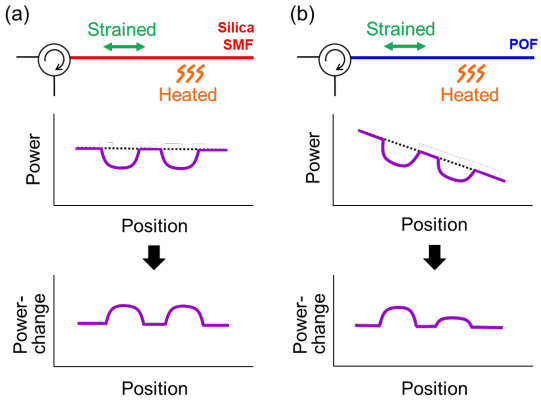

Fig. 7. Power and power-change distributions along (a) a low-loss fiber and (b) a high-loss POF; with (solid curves) and without (dotted lines) strain and heat.

4.1. POF-based operation

We made a trial to implement SA-BOCDR using a high-loss POF. We showed that, unlike low-loss silica fibers, the strain and temperature sensitivities are dependent on sensing position because the transmitted power gradually decreases in the POFs. After analyzing this unique effect experimentally, we showed that this effect can be compensated so that a correct POF-based distributed measurement can be performed using SA-BOCDR.

The Brillouin scattering properties in perfluorinated POFs have been well summarized in [79]. The optical propagation loss of this kind of POF is ~250 dB/km at 1550 nm. The BFS is ~2.8 GHz, and the strain and temperature coefficients of the BFS are –120 MHz/% and –3.2 MHz/K (which depend on samples). Some interesting phenomena of Brillouin scattering in POFs, such as a BFS hoping effect, have been reported, and the operation of POF-based BOCDR has been achieved [53,60].

The idea is presented in Fig. 7. When a silica SMF with a low propagation loss is used as an FUT, unless the FUT is extremely long, the Brillouin power shows almost no change irrespective of the sensing position. However, when a relatively high-loss fiber including a POF is used, even when the FUT is short, the Brillouin power decreases with increasing distance from the proximal end of the FUT. The

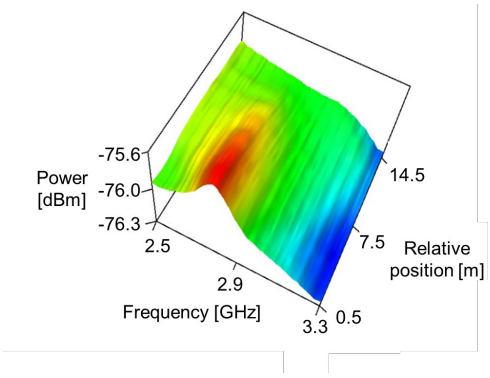

Fig. 8. BGS distribution along the POF.

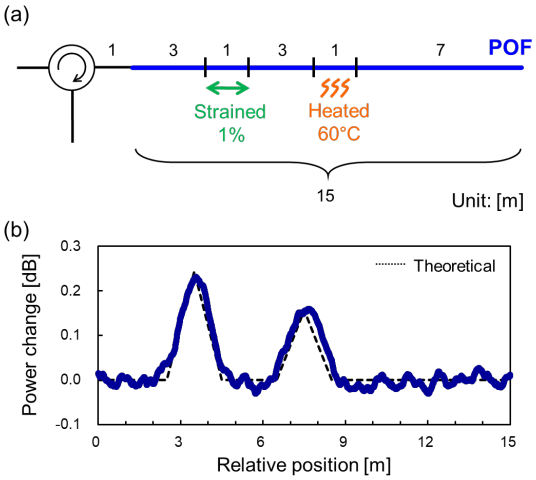

Fig. 9. (a) Structure of the POF under test. (b) Power-change distribution along the POF. The dotted line is a theoretical trend.

weakening of the BGS along the FUT leads to the reduction in the spectral slope, finally resulting in the gradual decrease in the strain and temperature sensitivities.

In the demonstration, we employed a 15.0-m-long POF. The measurement range was 18.1 m and the theoretical spatial resolution was 0.96 m. Refer to [74] for more detailed conditions. First, to derive the theoretical strain and temperature sensitivities as functions of sensing position, we measured the BGS distribution along the POF with a constant interval of 1.0 m using standard BOCDR (Fig. 8). The peak power of the BGS gradually decreased with light propagation, which also induced the reduction in its spectral slope. By analyzing this result carefully (refer to [74] for details), the temperature sensitivity was calculated as a function of sensing position, and the dependence coefficient was -4.98×10^{-4} dB/°C/m (corresponding to -2.10×10^{-2} dB/%/m for strain).

Then, we demonstrated distributed measurement of strain and temperature along the POF using SA-BOCDR. The structure of the FUT is depicted in Fig. 9(a). A 1.0-m-long section was strained for 1 %, and another 1.0-m-long section was heated to 60°C. The measured power-change distribution is shown in Fig. 9(b). At the expected sections, the power changes corresponding to the strain and the temperature change were observed, which moderately agrees with the theoretical dotted line considering the sensitivity dependence on sensing position and the trapezoidal effect of SA-BOCDR. Thus, the applied strain and temperature change along the POF were correctly detected.

4.2. Pseudo-field test

As a first step toward such practical applications, we presented an example of SA-BOCDR-based diagnosis using an optical fiber embedded in a composite structure [75]. As a specimen to be measured, we prepared a carbon fiber-reinforced plastic (CFRP) strengthened steel plate, in which a standard silica SMF was embedded. As load was applied to the structure on its top or bottom, we detected the induced compressive and tensile strain distributions, respectively. We showed that the breakage of the embedded fiber can also be detected as an abrupt local power change in the SA-BOCDR output.

Figure 10 shows the structure of the specimen. A 1.4-m-long silica SMF with BFS of 10.85 GHz was, as an FUT, embedded between a steel plate and CFRP strips. This structure was fabricated by placing the SMF before the infusing liquid resin during the vacuum-assisted resin transfer molding. The depth of the structure was 39 mm, and the thickness of the steel plate was 12 mm. The total thickness of the CFRP strips composed of seven tapered layers was ~3 mm.

We performed two different types of experiments:

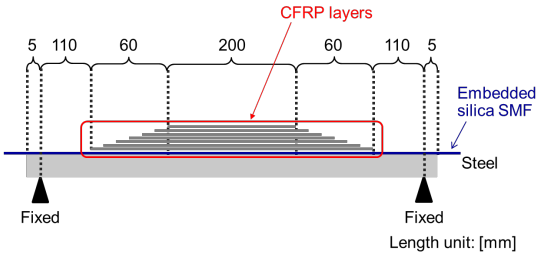

Fig. 10. Specimen structure.

one for evaluating the magnitude of tensile and compressive strains, and the other for detecting the fiber breakage. First, using a three-point bending device, tensile and compressive strains were applied to the middle of the specimen by tightening the top screw with a pitch of 2 mm. We measured the distributed tensile and compressive strains from 0 to 1.5 and from 0 to 2.5 turns (of the top screw), respectively. Measurements were performed every 0.5 turns. Finite-element analysis shows that the strain increases by ~400 με with each additional turn.

Similar experiments were performed by applying larger compressive strains to the specimen until the sensing fiber was broken. Using SA-BOCDR, the power-change distributions were measured while the top screw was tightened from 0 to 6.0 turns, corresponding to strains of 0 to ~2400 με. The room temperature was 23 °C. The measurement range was 11.3 m and the spatial resolution was 71 mm.

First, we present the experimental results of evaluating the magnitude of the applied tensile and compressive strains. Figure 11(a) shows the measured power-change distributions along the whole sensing fiber when tensile strains of 0, 200, 400, and 600 με and compressive strains of 0, 200, 400, 600, 800, and 1000 με were applied to the specimen. The vertical axis was converted into strain using the known strain-dependence coefficient of a power change of –1.59 dB/%. The horizontal axis indicates the relative distance from the midpoint of the embedded section of the sensing fiber. The power changes were observed along a ~390-mm-long section around the embedded section. With increasing applied tensile and compressive strains, the measured strains also increased moderately in accordance with the theoretical values. In Fig. 11 (b), the maximal strain obtained from each measured

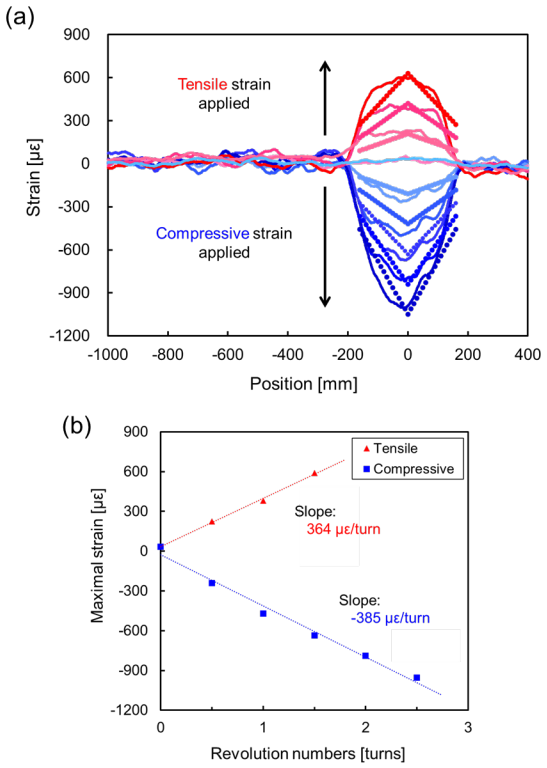

Fig. 11. (a) Strain distributions along the FUT measured at tensile strains of 0, 200, 400, and 600 με and compressive strains of 0, 200, 400, 600, 800, and 1000 με. The dotted lines are the theoretical trends. (b) Maximal tensile and compressive strains plotted in terms of the revolution numbers of the top screw.

distribution in Fig. 11(a) is plotted as a function of the number of revolutions of the top screw. Irrespective of tensile or compressive strains, the maximal strain increased almost linearly with increasing the number of revolutions of the screw. The calculated slopes for tensile and compressive strains were ~364 με/turn and ~385 με/turn, respectively, in a moderate agreement with theoretical values (~400 με/turn).

Subsequently, we detected the fiber breakage by applying larger compressive strains. The top screw was tightened to 0, 1.5, 3.0, 4.5, 5.3, 5.5, and 6.0 turns. The measured distributions of the power

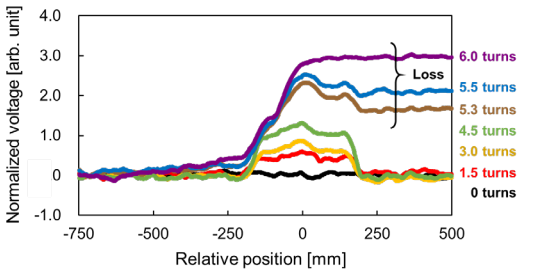

Fig. 12. Power-change distributions along the FUT measured when the compressive strains were applied till the FUT was broken.

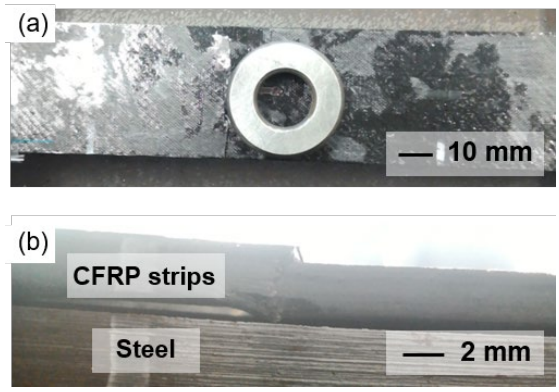

Fig. 13. Photographs of the CFRP strips peeled off from the steel; (a) top view and (b) side view.

change (output as voltage) are shown in Fig. 12. The vertical axis was defined to be positive when the strain was compressive. When the number of revolutions was equal to or smaller than 4.5, the power changes were observed along the correct section. In this range of strains, the power change was almost proportional to the number of revolutions. However, when the number of revolutions was larger than 5.3 (~2120 με), the power change showed a drastic increase along the distal side from the midpoint of the specimen. This behavior implies that considerable optical loss was induced. Figure 13 shows the photographs of the specimen after the revolution number of 6.0 turns was applied. Part of the CFRP strips were clearly peeled off from the steel. By directly measuring the transmitted optical power, we confirmed the breakage of the fiber itself. Thus, we showed that SA-BOCDR has a capability to indirectly predict the peeling of composite structures via fiber breakage detection.

4.3. >10-km-range operation

Almost all the previously reported demonstrations of BOCDR had measurement ranges shorter than ~1.5 km. If we exploit the beyond-nominal-resolution effect [68], it is feasible to detect a meter-order-long strained/heated section along a long FUT [76] even without the use of special configurations for extending measurement range, such as temporal gating and double modulation schemes [47,48].

In general, we need to employ a delay line in a reference path which should be at least 4 times longer than the FUT. In this long-range configuration, the use of such a long delay line inevitably accompanies forward-propagating Brillouin-scattered light in the reference path, which leads to a deteriorated SNR and should be filtered out.

The structure of the FUT is depicted in Fig. 14(a). A 13-km-long silica SMF with a BFS of 10.88 GHz was employed as an FUT, and a considerable bending loss was artificially applied near its end to suppress the Fresnel reflection. A 3-m-long section (11 km far from the proximal end) was heated from room temperature (23°C) to 70°C. The modulation amplitude was 5 GHz, and the modulation frequency was swept from 4.51 kHz to 7.07 kHz, corresponding to the measurement range of 14.5 km and the nominal spatial resolution from 26.7 m to 41.9 m.

The normalized power-change distributions near the heated section (23°C, 50°C, and 70°C) are shown in Fig. 14(b). Clear peaks were observed at the heated section. The shape of the waveforms at the heated section is not rectangular, which is valid considering the nature of SA-BOCDR. It is also valid that the peaks were broadened because the nominal spatial resolution at this position is 28.2 m. The SNR was not high in this long-range measurement, because (1) the incident power was much lower than those of shorter-range measurement, (2) the weak incident power was reduced further during propagation of the long FUT, (3) the measurement position is far beyond the coherence length of the laser (~100 m), and (4) the aforementioned noise caused by the Brillouin components in the reference path cannot be completely suppressed. Subsequently, we plotted the

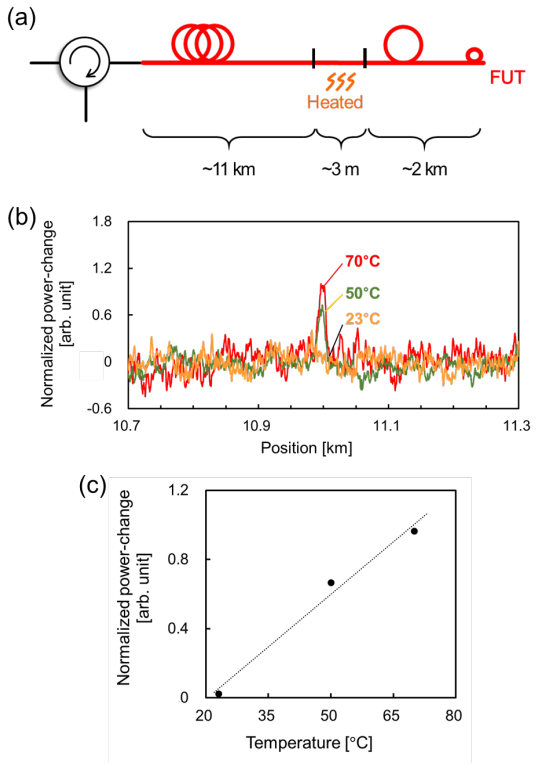

Fig. 14. (a) FUT structure. (b) Power-change distributions near the heated section. (c) Maximal power-change plotted as a function of temperature. The dotted line is a linear fit.

maximal power-change at the heated section as a function of temperature (Fig. 14(c)). The dependence was almost linear, indicating that, although the SNR was low, a 3-m-long heated section was properly detected at a >10 km distant position. By additionally employing the temporal gating scheme and/or the double modulation scheme, we may be able to extend the measurement range further while maintaining the short-hot-spot detectability.

4.4. Bending-loss-independent operation

The loss-sensitive nature is a unique feature of SA-BOCDR and can be exploited as described in Section 4.2. However, from the viewpoint of stable measurement of strain and temperature, the final output of SA-BOCDR should not be influenced by unintended loss applied to the FUT. One of our solutions was simple; we employed a special silica fiber with low bending loss [77].

The low-bending-loss silica fiber used in the experiment was a 12.0-m-long trench-index-type special SMF (FutureGuide-BIS-B, Fujikura) with a low bending loss (e.g., 0.018 dB/turn at 1550 nm for a bending radius of 7.5 mm). One end of this special fiber was connected to the 1.0-m-long pigtail of the second port of an optical circulator via an adaptor, and the other end was cut with an angle and immersed into index matching oil to suppress the Fresnel-reflection-dependent signal fluctuations.

Fundamental characterization revealed that the coefficients of the power-change dependencies on strain and temperature are 1.42×10^{-4} dB/με and 3.28×10^{-3} dB/K, respectively (when the spatial resolution is 144 mm and the measurement range is 14.7 m). As for the details, refer to [77]. The loss-insensitive operation of SA-BOCDR was demonstrated using the FUTs depicted in Fig. 15. Two different types of 12.0-m-long silica SMFs (a standard SMF (FPC-SM20, Alnair Labs) and the low-bending-loss SMF) were employed. Heat (70°C) and strain (400 με) were applied to 0.15-m-long sections, and bending losses were applied between the heated and strained sections. The bending loss was applied by winding the fibers around rods for one turn without strain. The radii of the rods were 8 and 10 mm, which theoretically induce bending losses of ~3.1 and ~0.8 dB for the standard SMF, respectively. The bending losses induced to the special SMF were relatively low (< 0.02 dB).

Figure 15(b) shows the power-change distributions measured along the standard SMF with 8- and 10-mm rod radii. The vertical axis was normalized so that the maximal power change at the heated section became 1 (when the rod radius was 10 mm). Note that the two distributions were displayed with an artificial shift of 2 for clear comparison. Regardless of the rod radii, the heated sections were correctly detected, and the rough locations of the applied bending losses were also detected. However, when the rod radius was 10 mm, the location of the strained section was correctly detected, but the strain magnitude appeared to be much smaller than the actual value (which is approximately 0.6). This is because the BGS power reduced by bending loss lead to the reduction in the spectral slope, resulting in the

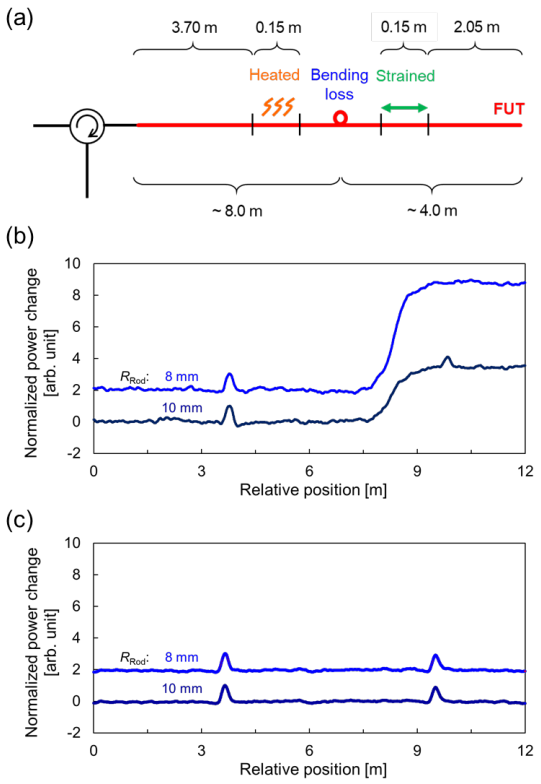

Fig. 15. (a) FUT structure, where heat, strain, and bending loss were applied. Power-change distributions with rod radii of 8 and 10 mm when the FUT was (b) the standard silica SMF and (c) the low-bending-loss silica SMF. Each distribution was shifted by 2.

reduced sensitivity to strain. When the rod radius was even smaller (8 mm), the loss was so high that the strained section was not detected at all. This is because the considerable loss almost completely diminished the BGS (i.e., the spectral slope became almost flat), and consequently, the strain-induced spectral shift posed only negligible influence on the final output. In contrast, Fig. 15(c) shows the normalized power-change distributions measured along the low-bending-loss SMF with 8- and 10-mm rod radii. The two distributions were similar to each other irrespective of the rod radii, and the heated and strained sections were correctly detected in both measurements. The applied bending losses did not affect the measured results, indicating that, by SA-BOCDR using this special fiber, a stable distributed measurement of strain and temperature can be performed with no influence of unintended local loss.

4.5. Sensitivity/sensitivity-enhanced operation

One of the major drawbacks of power-based operation of SA-BOCDR is the significant polarization-dependent power fluctuations, which lead to unstable operation of the system. To date, to mitigate this noise, a PSCR has been employed in the system, but the averaged state of polarization (SOP) leads to non-ideal sensitivity, and in addition, the use of the PSCR increases the cost and encumbers the downsizing of the system. Polarization diversity has also been employed in BOCDR, but the negative situation cannot be remedied because of the use of a polarization switch, and what is worse, the sampling rate inevitably becomes less than half for data processing. To resolve these shortcomings, we develop polarization-scrambling-free SA-BOCDR using a polarization-maintaining fiber (PMF) as an FUT. A PSCR is not employed in this configuration, leading to the cost reduction (when the FUT is relatively short). In addition, what is more important, the SOP can be optimized so that the sensitivity can be higher, as a higher-power BGS has a larger slope, resulting in a higher sensitivity. As for the details, refer to [78], where the demonstration movie of real-time distributed temperature sensing using a PMF is also available.

4.6. Polarization beat length measurement

Distributed measurement of polarization beat length (birefringence) along an optical fiber is of great interest in the recent high-speed fiber-optic communication with a transmission rate of >100 Gbps. Polarization-sensitive optical time-domain reflectometry (POTDR) [80] is a simple technique based on Rayleigh-scattered polarized light, but it has lower spatial resolution and longer measurement time. Polarization-sensitive optical frequency-domain reflectometry (POFDR) [81] is also a technique for measuring the beat length distributions with extremely high resolution, but the measurement range was strictly limited. As another approach, the polarization dependence of Brillouin scattering has

also been used to measure the beat length distributions along optical fibers. Using BOCDA, a high spatial resolution of 2.7 cm was achieved. However, light injection to both ends of the FUT is not convenient in long-range applications. Single-end-access distributed beat length measurement was demonstrated on the basis of BOCDR [63], and a spatial resolution of 25 cm and a sampling rate of 20 Hz were obtained. However, it was time-consuming to switch the system from beat length sensing mode to strain/temperature sensing mode, and vice versa. To overcome this issue, we have recently demonstrated distributed beat length measurement based on SA-BOCDR. In addition to the advantages of single-end accessibility, high spatial resolution, high speed measurement, and cost efficiency, the SA-BOCDR-based method has a unique advantage that the measurands can be easily changed from beat length to strain/temperature by switching on a PSCR used in the system. The experimental results will be soon published.

5. Discussion and Conclusion

We presented a review on the recent progress in the SA-BOCDR technology. Since the first proposal in 2016 [67], its unique features have been characterized, and some applications and demonstrations have been provided. The basic motivation of this technique was to boost the operating speed of a standard BOCDR system, but a number of other aspects have also been improved or discovered somewhat accidentally. However, SA-BOCDR still suffers from two major technical issues.

One is the inherently low stability of the system caused by the direct use of optical spectral power. For instance, if the output power of the light source fluctuates, or if unexpected loss is applied to the fiber before the proximal end of the FUT, the system output is inevitably influenced, leading to erroneous strain and temperature measurement. One solution may be to utilize two or more frequency components simultaneously [15]. For instance, if we employ the power ratio of the two frequency components, it will be free from the aforementioned errors. These frequency components could be either in the same slope or in different slopes. The lowered strain (or temperature) dynamic range will be its trade-off, but it might be mitigated by a peak-tracing technique, etc.

The other problem is the possible measurement error caused by the BGS shape modified by the irregular strain (or temperature) distribution in the vicinity of the sensing point. The BGS observed by correlation-domain techniques is generally composed of two spectral contributions, i.e., the sharp signal peak corresponding to the measured strain and the noise structure caused by scattering from all the other positions. Consequently, even if the peak frequency is maintained, the BGS shape may be modified by the strain distribution at the positions near the correlation peak [38]. This neighborhood effect has been well clarified in the case of PD-BOCDR [61], in which the measurement can be correctly performed if some deterioration of spatial resolution is permitted (for instance, ~3 times). This discussion should hold true in SA-BOCDR, but the quantitative evaluation needs to be independently conducted and is one of the important future tasks.

Despite these issues to be solved, they never change the fact that SA-BOCDR is the useful technology with unique advantages of operation by single-end light injection, random accessibility to measuring points, and real-time operation. A special configuration that possesses the advantages of both SA-BOCDR and standard BOCDR will be feasible, considering the similarity of their setups. Thus, we anticipate that SA-BOCDR will be one of the promising key techniques for Brillouin-based distributed sensing in the future.

Declaration of Competing Interest

The authors declare that they have no known competing financial interests or personal relationships that could have appeared to influence the work reported in this paper.

Acknowledgment

This work was partly supported by JSPS KAKENHI Grant Numbers 17H04930 and 17J07226 and by research grants from the Noguchi Institute and the Telecommunications Advancement Foundation.

References

[1] G.P. Agrawal, Nonlinear Fiber Optics, Academic Press, California, 1995.

[2] T. Horiguchi, M. Tateda, BOTDA—Nondestructive measurement of single-mode optical fiber attenuation characteristics using Brillouin interaction: Theory, J. Lightwave Technol. 7 (1989) 1170–1176.

[3] X.H. Jia, Y.J. Rao, L. Chang, C. Zhang, Z.L. Ran, Enhanced sensing performance in long distance Brillouin optical time-domain analyzer based on Raman amplification: theoretical and experimental investigation, J. Lightwave Technol. 28 (2010) 1624–1630.

[4] D. Zhou, Y. Dong, B. Wang, C. Pang, D. Ba, H. Zhang, Z. Lu, H. Li, X. Bao, Single-shot BOTDA based on an optical chirp chain probe wave for distributed ultrafast measurement, Light: Sci. Appl. 7 (2018) 32.

[5] C. Kito, H. Takahashi, K. Toge, T. Manabe, Dynamic strain measurement of 10-km fiber with frequency-swept pulsed BOTDA, J. Lightwave Technol. 35 (2017) 1738–1743.

[6] M.A. Soto, J.A. Ramírez, L. Thévenaz, Intensifying the response of distributed optical fibre sensors using 2D and 3D image restoration, Nature Commun. 7 (2016) 10870.

[7] Y. Dong, H. Zhang, L. Chen, X. Bao, 2 cm spatial-resolution and 2 km range Brillouin optical fiber sensor using a transient differential pulse pair, Appl. Opt. 51 (2012) 1229–1235.

[8] A.K. Azad, L. Wang, N. Guo, H.Y. Tam, C. Lu, Signal processing using artificial neural network for BOTDA sensor system, Opt. Express 24 (2016) 6769–6782.

[9] A. Motil, R. Davidi, R. Hadar, M. Tur, Mitigating the effects of the gain-dependence of the Brillouin line-shape on dynamic BOTDA sensing methods, Opt. Express 25 (2017) 22206–22218.

[10] D. Marini, M. Iuliano, F. Bastianini, G. Bolognini, BOTDA sensing employing a modified Brillouin fiber laser probe source, J. Lightwave Technol. 36 (2018) 1131–1137.

[11] D. Zhou, Y. Dong, B. Wang, T. Jiang, D. Ba, P. Xu, H. Zhang, Z. Lu, H. Li, Slope-assisted BOTDA based on vector SBS and frequency-agile technique for wide-strain-range dynamic measurements, Opt. Express 25 (2017) 18890–1902.

[12] Y. Peled, A. Motil, L. Yaron, M. Tur, Slope-assisted fast distributed sensing in optical fibers with arbitrary Brillouin profile, Opt. Express 19 (2011) 19845–19854.

[13] X. Tu, H. Luo, Q. Sun, X. Hu, Z. Meng, Performance analysis of slope-assisted dynamic BOTDA based on Brillouin gain or phase-shift in optical fibers, J. Opt. 17 (2015) 105503.

[14] A. Minardo, A. Coscetta, R. Bernini, L. Zeni, Heterodyne slope-assisted Brillouin optical time-domain analysis for dynamic strain measurements, J. Opt. 18 (2016) 025606.

[15] D. Ba, B. Wang, D. Zhou, M. Yin, Y. Dong, H. Li, Z. Lu, Z. Fan, Distributed measurement of dynamic strain based on multi-slope assisted fast BOTDA, Opt. Express 24 (2016) 9781–9793.

[16] A.H. Hartog, F.V. Englich, Non-linear interactions with backscattered light: a truly single-ended Brillouin optical time-domain analysis technique, J. Lightwave Technol. 37 (2019) 2386–2402.

[17] D. Zhou, Y. Dong, B. Wang, C. Pang, D. Ba, H. Zhang, Z. Lu, H. Li, X. Bao, Single-shot BOTDA based on an optical chirp chain probe wave for distributed ultrafast measurement Light: Sci. Appl. 7 (2018) 32.

[18] T. Kurashima, T. Horiguchi, H. Izumita, S. Furukawa, Y. Koyamada, Brillouin optical-fiber time domain reflectometry, IEICE Trans. Commun. E76-B **(**1993) 382–390.

[19] M.N. Alahbabi, Y.T. Cho, T.P. Newson, 100 km distributed temperature sensor based on coherent detection of spontaneous Brillouin backscatter, Meas. Sci. Technol. 15 (2004) 1544–1547.

[20] Y. Koyamada, Y. Sakairi, N. Takeuchi, S. Adachi, Novel technique to improve spatial resolution in Brillouin optical time-domain reflectometry. IEEE Photonics Technol. Lett. 19 (2007) 1910–1912.

[21] F. Wang, C. Zhu, C. Cao, X. Zhang, Enhancing the performance of BOTDR based on the combination of FFT technique and complementary coding, Opt. Express 25 (2017) 3504–3513.

[22] K. Koizumi, Y. Kanda, A. Fujii, H. Murai, High-speed distributed strain measurement using Brillouin optical time-domain reflectometry based-on self-delayed heterodyne detection, Proc. 41st European Conference on Optical Communication (ECOC2015), Valencia, Spain, 27 Sep.–1 Oct. 2015.

[23] Y. Hao, K. Yang, N. Liu, S. Liu, F. Zhai, Suppression of amplitude fluctuation in Brillouin optical fiber reflectometry employing polarization beam splitter and pre-amplification technique, Optical Fiber Technology 57 (2020) 102217.

[24] A. Zafeiropoulou, A. Masoudi, A. Zdagkas, L. Cooper, G. Brambilla, Curvature sensing with a D-shaped multicore fibre and Brillouin optical time-domain reflectometry, Opt. Express 28 (2020) 1291–1299.

[25] Q. He, H. Jiang, Z. Wang, S. Ye, X. Shang, T. Li, L. Tang, Spatial resolution enhancement of DFT-BOTDR with high-order self-convolution window, Optical Fiber Technology 57 (2020) 102188.

[26] K. Hotate, T. Hasegawa, Measurement of Brillouin gain spectrum distribution along an optical fiber using a correlation-based technique—Proposal, experiment and simulation, IEICE Trans. Electron. E83-C (2000) 405–412.

[27] K.Y. Song, M. Kishi, Z. He, K. Hotate, K. High-repetition-rate distributed Brillouin sensor based on optical correlation-domain analysis with differential frequency modulation. Opt. Lett. 36 (2011) 2062–2064.

[28] C. Zhang, M. Kishi, K. Hotate, 5,000 points/s high-speed random accessibility for dynamic strain measurement at arbitrary multiple points along a fiber by Brillouin optical correlation domain analysis, Appl. Phys. Express 8 (2015) 042501.

[29] B. Wang, X. Fan, Y. Fu, Z. He, Dynamic strain measurement with kHz-level repetition rate and centimeter-level spatial resolution based on Brillouin optical correlation domain analysis, Opt. Express 26 (2018) 6916–6928.

[30] W. Zou, C. Jin, J. Chen, Distributed strain sensing based on combination of Brillouin gain and loss effects in Brillouin optical correlation domain analysis, Appl. Phys. Express 5

(2012) 082503.
[31] G. Ryu, G. Kim, K.Y. Song, S.B. Lee, K. Lee, Brillouin optical correlation-domain analysis enhanced by time-domain data processing for concurrent interrogation of multiple sensing points, J. Lightwave Technol. 35 (2017) 5311–5316.
[32] A. Denisov, M.A. Soto, L. Thévenaz, Going beyond 1000000 resolved points in a Brillouin distributed fiber sensor: theoretical analysis and experimental demonstration, Light: Sci. Appl. 5 (2016) e16074.
[33] Y. London, Y. Antman, E. Preter, N. Levanon, A. Zadok, Brillouin optical correlation domain analysis addressing 440,000 resolution points, J. Lightwave Technol. 34 (2016) 4421–4429.
[34] A. López-Gil, S. Martin-Lopez, M. Gonzalez-Herraez, Phase-measuring time-gated BOCDA, Opt. Lett. 42 (2017) 3924–3927.
[35] J. Zhang, M. Zhang, M. Zhang, Y. Liu, C. Feng, Y. Wang, Y. Wang, Chaotic Brillouin optical correlation-domain analysis, Opt. Lett. 43 (2018) 1722–1725.
[36] E. Preter, D. Ba, Y. London, O. Shlomi, Y. Antman, A. Zadok, High-resolution Brillouin optical correlation domain analysis with no spectral scanning, Opt. Express 24 (2016) 27253–27267.
[37] Y. Okawa, R. K. Yamashita, M. Kishi, K. Hotate, Analysis of Brillouin dynamic grating localized by intensity-modulated correlation-domain technique for distributed fiber sensing, Opt. Express 28 (2020) 6981–6994.
[38] K.Y. Song, Z. He, K. Hotate, Effects of intensity modulation of light source on Brillouin optical correlation domain analysis, J. Lightwave Technol. 25 (2017) 1238–1246.
[39] Y. Wang, M. Zhang, J. Zhang, L. Qiao, T. Wang, Q. Zhang, L. Zhao, Y. Wang, Millimeter-level-spatial-resolution Brillouin optical correlation-domain analysis based on broadband chaotic laser, J. Lightwave Technol. 37 (2019) 3706–3712.
[40] B. Wang, X. Fan, Y. Fu, Z. He, Enhancement of strain/temperature measurement range and spatial resolution in Brillouin optical correlation domain analysis based on convexity extraction algorithm, IEEE Access (2019) 32128–32136.
[41] Y. Mizuno, W. Zou, Z. He, K. Hotate, Proposal of Brillouin optical correlation-domain reflectometry (BOCDR), Opt. Express 16 (2008) 12148–12153.
[42] Y. Mizuno, H. Lee, K. Nakamura, Recent advances in Brillouin optical correlation-domain reflectometry, Appl. Sci. 8 (2018) 1845.
[43] Y. Mizuno, W. Zou, Z. He, K. Hotate, Operation of Brillouin optical correlation-domain reflectometry: theoretical analysis and experimental validation, J. Lightwave Technol. 28 (2010) 3300–3306.
[44] Y. Mizuno, W. Zou, Z. He, K. Hotate, One-end-access high-speed distributed strain measurement with 13-mm spatial resolution based on Brillouin optical correlation-domain reflectometry, IEEE Photonics Technol. Lett. 21 (2009) 474–476.
[45] Y. Mizuno, Z. He, K. Hotate, Distributed strain measurement using a tellurite glass fiber with Brillouin optical correlation-domain reflectometry, Opt. Commun. 283 (2010) 2438–2441.
[46] S. Manotham, M. Kishi, Z. He, K. Hotate, 1-cm spatial resolution with large dynamic range in strain distributed sensing by Brillouin optical correlation domain reflectometry based on intensity modulation, Proc. 3rd Asia Pacific Optical Sensors Conference (APOS2012), Sydney, Australia, 31 Jan.-3 Feb. 2012; SPIE 8351 (2012) 835136.
[47] Y. Mizuno, Z. He, K. Hotate, Measurement range enlargement in Brillouin optical correlation-domain reflectometry based on temporal gating scheme, Opt. Express 17 (2009) 9040–9046.
[48] Y. Mizuno, Z. He, K. Hotate, Measurement range enlargement in Brillouin optical correlation-domain reflectometry based on double-modulation scheme, Opt. Express 18 (2010) 5926–5933.
[49] K. Noda, H. Lee, K. Nakamura, Y. Mizuno, Measurement range enlargement in Brillouin optical correlation-domain reflectometry based on chirp-modulation scheme, Appl. Phys. Express 13 (2020) 082003.
[50] Y. Mizuno, Z. He, K. Hotate, Stable entire-length measurement of fiber strain distribution by Brillouin optical correlation-domain reflectometry with polarization scrambling and noise-floor compensation, Appl. Phys. Express 2 (2009) 062403.
[51] N. Hayashi, Y. Mizuno, K. Nakamura, Suppression of ghost correlation peak in Brillouin optical correlation-domain reflectometry, Appl. Phys. Express 7 (2014) 112501.
[52] N. Hayashi, K. Minakawa, Y. Mizuno, K. Nakamura, Polarization scrambling in Brillouin optical correlation-domain reflectometry using polymer fibers, Appl. Phys. Express 8 (2015) 062501.
[53] Y. Mizuno, H. Lee, N. Hayashi, K. Nakamura, Noise suppression technique for distributed Brillouin sensing with polymer optical fibers, Opt. Lett. 44 (2019) 2097–2100.
[54] Y. Mizuno, N. Hayashi, H. Fukuda, K. Nakamura, Single-end-access distributed strain sensing with wide dynamic range using higher-speed Brillouin optical correlation-domain reflectometry, Jpn. J. Appl. Phys. 56 (2017) 072501.
[55] N. Hayashi, Y. Mizuno, K. Nakamura, Simplified configuration of Brillouin optical correlation-domain reflectometry, IEEE Photonics J. 6 (2014) 6802807.
[56] N. Hayashi, Y. Mizuno, K. Nakamura, Alternative implementation of simplified Brillouin optical correlation-domain reflectometry, IEEE Photonics J. 6 (2014) 6803108.
[57] N. Hayashi, Y. Mizuno, K. Nakamura, Simplified Brillouin optical correlation-domain reflectometry using polymer optical fiber, IEEE Photonics J. 7 (2015) 6800407.
[58] Y. Mizuno, G. Han, K. Noda, H. Lee, K. Nakamura, Low-cost Brillouin optical correlation-domain reflectometry involving merely one fibre amplifier, Electron. Lett. 55 (2019) 754–756.
[59] Y. Mizuno, N. Motoishi, K. Noda, H. Lee, K. Nakamura, Effect of laser temperature control on Brillouin optical correlation-domain reflectometry, Appl. Phys. Express 13 (2020) 052001.
[60] N. Hayashi, Y. Mizuno, K. Nakamura, Distributed Brillouin sensing with centimeter-order spatial resolution in polymer optical fibers, J. Lightwave Technol. 32 (2014) 3999–4003.
[61] Y. Mizuno, N. Hayashi, H. Fukuda, K.Y. Song, K. Nakamura,

Ultrahigh-speed distributed Brillouin reflectometry, Light: Sci. Appl. 5 (2016) e16184.
[62] Y. Mizuno, N. Hayashi, H. Fukuda, K. Nakamura, Phase-detected Brillouin optical correlation-domain reflectometry, Opt. Rev. 25 (2018) 473–485.
[63] Y. Mizuno, Z. He, K. Hotate, Polarization beat length distribution measurement in single-mode optical fibers with Brillouin optical correlation-domain reflectometry, Appl. Phys. Express 2 (2009) 046502.
[64] Y. Yao, M. Kishi, K. Hotate, Brillouin optical correlation domain reflectometry with lock-in detection scheme, Appl. Phys. Express 9 (2016) 072501.
[65] K. Noda, H. Lee, Y. Mizuno, K. Nakamura, First demonstration of Brillouin optical correlation-domain reflectometry based on external modulation scheme, Jpn. J. Appl. Phys. 58 (2019) 068004.
[66] K. Hotate, Z. He, Synthesis of Optical-coherence function and its applications in distributed and multiplexed optical sensing, J. Lightwave Technol. 24 (2006) 2541–2557.
[67] H. Lee, N. Hayashi, Y. Mizuno, K. Nakamura, Slope-assisted Brillouin optical correlation-domain reflectometry: proof of concept, IEEE Photon. J. 8 (2016) 6802807.
[68] H. Lee, N. Hayashi, Y. Mizuno, K. Nakamura, Operation of slope-assisted Brillouin optical correlation-domain reflectometry: comparison of system output with actual frequency shift distribution, Opt. Express 24 (2016) 29190–29197.
[69] H. Lee, Y. Mizuno, K. Nakamura, Detection of 2-mm-long strained section in silica fiber using slope-assisted Brillouin optical correlation-domain reflectometry, Jpn. J. Appl. Phys. 57 (2018) 020303.
[70] H. Lee, Y. Mizuno, K. Nakamura, Measurement sensitivity dependencies on incident power and spatial resolution in slope-assisted Brillouin optical correlation-domain reflectometry, Sens. Actuat. A: Phys. 268 (2017) 68–71.
[71] H. Lee, K. Noda, Y. Mizuno, K. Nakamura, Trade-off relation between strain dynamic range and spatial resolution in slope-assisted Brillouin optical correlation-domain reflectometry, Meas. Sci. Technol. 30 (2019) 075204.
[72] R. Kashyap, The fiber fuse - from a curious effect to a critical issue: a 25th year retrospective, Opt. Express 21 (2013) 6422–6441.
[73] Y. Mizuno, N. Hayashi, H. Tanaka, K. Nakamura, S. Todoroki, Observation of polymer optical fiber fuse, Appl. Phys. Lett. 104 (2014) 043302.
[74] H. Lee, N. Hayashi, Y. Mizuno, K. Nakamura, Slope-assisted Brillouin optical correlation-domain reflectometry using polymer optical fibers with high propagation loss, J. Lightwave Technol. 35 (2017) 2306–2310.
[75] H. Lee, Y. Ochi, T. Matsui, Y. Matsumoto, Y. Tanaka, H. Nakamura, Y. Mizuno, K. Nakamura, Distributed strain measurement and possible breakage detection of optical-fiber-embedded composite structure using slope-assisted Brillouin optical correlation-domain reflectometry, Appl. Phys. Express, 11 (2018) 072501.
[76] H. Lee, K. Noda, Y. Mizuno, K. Nakamura, Distributed temperature sensing based on slope-assisted Brillouin optical correlation-domain reflectometry with over 10 km measurement range, Electron. Lett. 55 (2019) 276–278.
[77] H. Lee, T. Ma, Y. Mizuno, K. Nakamura, Bending-loss-independent operation of slope-assisted Brillouin optical correlation-domain reflectometry, Sci. Rep. 8 (2018) 7844.
[78] H. Lee, Y. Mizuno, K. Nakamura, Enhanced stability and sensitivity of slope-assisted Brillouin optical correlation-domain reflectometry using polarization-maintaining fibers, OSA Contin. 2 (2019) 874–880.
[79] Y. Mizuno, N. Hayashi, K. Nakamura, Distributed Brillouin Sensing Using Polymer Optical Fibers, in: H. Alemohammad (Ed.), Opto-Mechanical Fiber Optic Sensors: Research, Technology, and Applications in Mechanical Sensing, Elsevier, Oxford, 2018, Ch. 5, 97–135.
[80] A.J. Rogers, Polarization-optical time domain reflectometry: a technique for the measurement of field distributions, Appl. Opt. 20 (1981) 1060–1074.
[81] J.P. Von der Weid, R. Passy, G. Mussi, N. Gisin, On the characterization of optical fiber network components with optical frequency domain reflectometry, J. Lightwave Technol. 15 (1997) 1131–1141.